Measurement-Based Large-Scale Propagation Characterization in 5G Micro-Cells At 3.8 GHz

Julian David Villegas Gutierrez, *Member, IEEE*, and Claude Oestges, *Fellow, IEEE*

***Abstract*—Large-scale propagation characterization for multiple measurements in a micro-cell scenario is carried out at 5G frequency (3.8 GHz). Distance-based path loss is computed for routes with line-of-sight, non-line-of-sight and obstructed-line-of-sight conditions, assuming a simple power law model. Path Loss exponents are computed for the whole routes, giving an effective understanding of the propagation environment. Empirical shadowing distribution is fitted to red Gaussian and non-Gaussian probability distributions. All previous propagation parameters are also found assuming measurements with similar transmitter locations come from the same channel conditions. This assumption is tested. Finally, although frequently absent in standard channel models, and useful for statistical ensemble average approximations, stationary regions are computed for all the routes.**

***Index Terms*—Propagation, wireless radio channel, measurements, 5G, shadowing, path loss.**

I. Introduction

LARGE-scale propagation is responsible for the variation of the received power (or equivalently, signal strength) due to distance and obstacles. It is an unavoidable step in link budget computations to serve users, while satisfying power constraints. Such computations could be possible thanks to measurements providing realistic channel information. However, to be able to replicate results, models for large scale propagation variables as distance-based path loss and shadowing have been red proposed by the Mobile and wireless communications Enablers for the Twenty-twenty Information Society (METIS) [1], the european COoperation in Science and Technology Action 2100 (COST2100) [2], [3], the 3rd Generation Partnership Project (3GPP) [4]–[6] and the Fraunhofer Institute for Telecomunications with their QUAsi Deterministic RadIo channel GenerAtor (QuaDRiGa) red [7], among others. Those models are validated through extensive measurement campaigns (a survey of which is presented in [8]), for which statistical parameters are computed, dividing models, or the characteristics of the propagation, by environment (urban, semi-urban,...), frequency intervals, Base Station (BS) antenna heights, and more. Some of the path loss models available in the mentioned references, and others, were developed for mobile communications that mostly operate up to 2 GHz [9]. For the 3.8 GHz frequency the available measurements are scarce ([10], at 3.5 GHz see [11], [12]) and the measurement setup (bandwidth, height of antennas) vary.

Besides so, not enough measurements have been carried out to cover the wireless channel behaviour in many types of scenario with similar used values of central frequency, bandwidth, antennas height. It means that any effort to extract parameters from well-known models (like the path loss) at different scenario locations is useful. That is because, not only there are no two scenarios with the same characteristics, but because under the same scenario the wireless channel might behave in a different way due to its variation with time. In addition to that, the purpose of measurement campaigns is to enlarge the database of parameters of established models (as the path-loss) to search for similarities such that the very large set of possible scenarios could be grouped into some categories (i.e. suburban micro-cell, rural macro-cell.

The purpose of this paper is framed within such efforts. A measurement campaign has been carried out in a micro-cell with suburban an rural characteristics, according to [13] classification: on one side there are non-negligible fluctuations of the terrain, and on the other side, building heights are a mixture of residential sizes plus multiple-floor university buildings.

The originality of this paper remains in the computation of the stationary regions and the discussion about the propagation conditions within them. This is among the first papers to present a computation for such regions, to our knowledge. Such regions in conjunction with directional information (i.e. Angles of Arrival and Angles of Departure) are useful to determine mechanisms of propagation (i.e. rooftop propagation, LoS, NLoS) over some space locations [14]. In other words, they provide a qualitative idea of what is happening in an scenario. Furthermore, stationary regions are required, for example, for the averaging step of the instantaneous Power Delay Profile (PDP): PDP estimation requires averaging over consecutive snapshots of the Channel Impulse Response (CIR). This is due to the fact that it is not feasible to have enough simultaneous measurements (realizations) of the same channel, and so, ergodicity assumed, ensemble averages are replaced by time averages. This window of consecutive snapshots should be long enough for the estimation to have low variance, and short enough such that channel characteristics have not change dramatically. Although, usually not included in previous cited models, stationary regions

Manuscript received 12 July 2021; revised 21 December 2021 and 28 April 2022; accepted 2 June 2022. Date of publication 14 July 2022; date of current version 14 November 2022. This work was supported by the SWIPT Project through UCLouvain ARC Program. It was also carried out in the framework of COST Action CA15104 IRACON. The review of this article was coordinated by Prof. Arafat J Al-Dweik. *(Corresponding authors: Julian David Villegas Gutierrez; Claude Oestges.)*

Julian David Villegas Gutierrez is with the Antennas Group, VTT, 02150 Espoo, Finland (e-mail: julian.villegas@vtt.fi).

Claude Oestges is with the ICTEAM, UCLouvain, 1348 Louvain-la-Neuve, Belgium (e-mail: claude.oestges@uclouvain.be).

Digital Object Identifier 10.1109/TVT.2022.3188345

play the role of providing this set of consecutive snapshots, for which the estimation of the PDP is reliable under the restrictions said before. This article tackles the problem of estimating those regions.

The article is organized as follows. In Section II, details about the measurement campaign setup are presented. In Section III, distance-based path loss models are presented, while parameters of the models are extracted from the measurements. Section IV deals with shadowing extraction and tests for its empirical distribution. Section V explains methodology to find out stationary regions, and results for such procedure. Finally, the article is closed with some conclusions in Section VI.

II. Measurement Campaing Setup

Measurement campaigns were carried out in Louvain-la-Neuve, Belgium. There were 2 static BS: one on top of the Mercator (in what follows abbreviated as MKT) building and the other on top of the Maxwell (in what follows abbreviated as MXW) building. For each BS there were 3 routes considered: around the Saint Barbe (SB) building, around the Marie Curie (MC) and Pierre Curie buildings (from now and on Marie Curie route), and around the Parking Lot (PL) below the SB building. For each route, there was 1 or more measurements (trials) done. All previously mentioned buildings are highlighted in Fig. 3 with all the other buildings composing the scenario under consideration.

Figs. 4 and 5 show the coordinates for the Mobile Station (MS) and the BS for all the measurements. For some of the graphs, anomalies could be seen regarding the MS movement (i.e. route comes in and out from building contour). This is due to the red Global Positioning System (GPS) system used. We tried to be as loyal as possible to the GPS coordinates measured by the channel sounder system. Linear interpolation is used between time-consecutive available GPS coordinates of the MS, so that for each CIR measured there is an associated GPS coordinate for the MS. The maximum distances between the MXW BS and the MS moving around the SB, MC and PL areas, were 225, 256 and 212 m, respectively. On the other hand, the minimum distances were 128, 187 and 144 m, respectively. The maximum distances between the MKT BS and the associated SB, MC and PL areas, were 191, 203 and 250 m, respectively. Equivalently, the minimum distances were 97, 125 and 183 m, respectively. The MS was moved by a trolley at an average speed of 1 $\frac{\mathrm{m}}{\mathrm{s}}$. A picture of both the MS (with the trolley) and the BS are shown in Fig. 1.

The measurement device used to sense the channel was the Propsound$^{\mathrm{TM}}$ Channel Sounder by Elektrobit. It sends a pseudo-random sequence that is the correlated with the received signal, to compute the CIR. At both ends of the communication system, Receiver (RX) and Transmitter (TX), there are antenna arrays. The channel sounder sends the sequence through all the antenna array elements, by fastly switching the connection between the TX component before the antenna array and each antenna array element. More information about the sounding signal characteristics is displayed in Table I. For the BS was used a 4-elements dual-polarized planar array with orthogonal slanted

Fig. 1. Photo of the BS and the MS used for the measurement campaing. Left: MS. Right: BS.

TABLE I
Sounding Signal Characteristics

Code Length	5.11 μs
Samples per Code (N_τ)	2044
CIR repetition rate (f_{IRF})	30.2 Hz
Center frequency (f_{c})	3.8 GHz
Bandwidth (B)	200 MHz

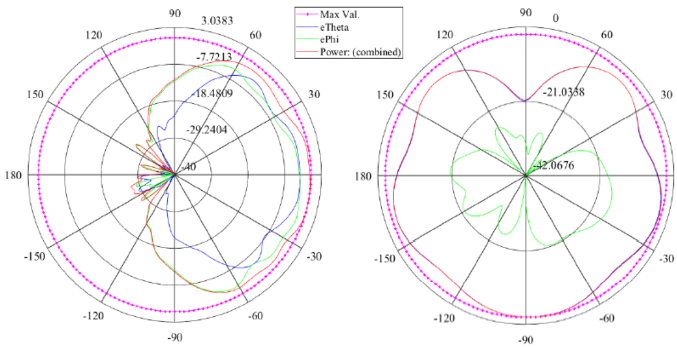

Fig. 2. Azimuthal antenna patterns of 1 element of the RX and TX antenna arrays. Left: double-polarized antenna. The convention ePhi and eTheta in the legend designate the $\mp\frac{\pi}{4}$ rad orthogonal polarization. Right: UCA. The convention ePhi and eTheta in the legend designate the horizontal and vertical polarizations, respectively.

polarizations. Therefore, the wireless communication system is a 8×8 Multiple Input Multiple Output (MIMO) system. For the MS was used an Uniform Circular Array (UCA) with 8 vertically polarized dipoles: 7 in the circumference and 1 in the center. In Fig. 2 the azimuthal antenna patterns of both arrays are shown.

The terrain is not regular: there are three noticeable ramps, besides the fact that MKT building is at a lower terrain height than the rest of buildings highlighted in Fig. 3. Transmitter antenna height is around 2 m. For the MXW antenna its height is above all the buildings (at an approximate height of 15 m). For the MKT antenna, the height is comparable to some of the buildings, since the building is at a lower terrain.

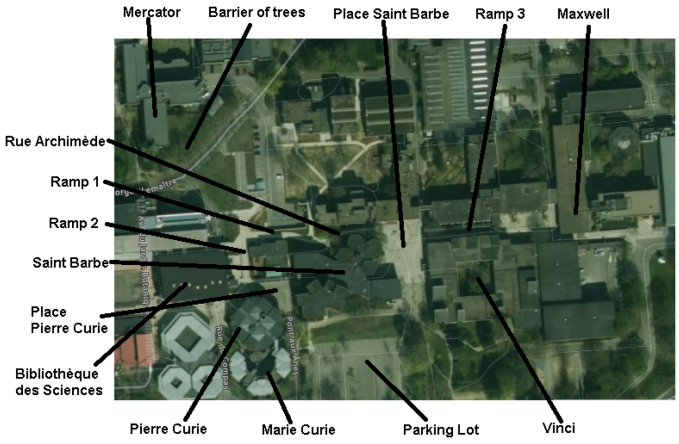

Fig. 3. Top view of buildings surrounding transmitter routes.

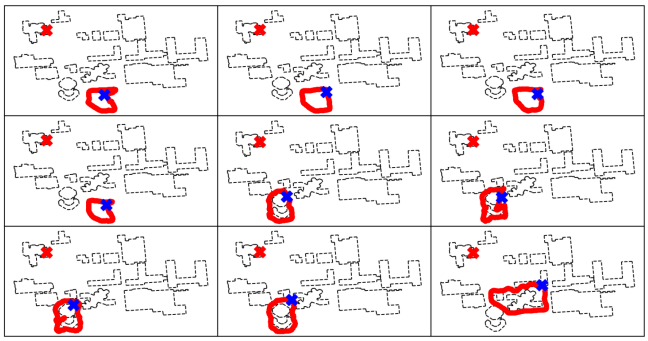

Fig. 4. Top view of transmitter measurement routes for MKT BS. The BS location, start of the route are indicated by the red cross and blue cross, respectively. By convention we designate graph in the top left as the graph (1,1). The convention used is: (row number, column number). Graph (1,1): PL route. Graph (1,2): PL route. Graph (1,3): PL route. Graph (2,1): PL route. Graph (2,2): MC route. Graph (2,3): MC route. Graph (3,1): MC route. Graph (3,2): MC route. Graph (3,3): SB route.

III. Distance-Based Path Loss

Beyond free space losses, arising from electromagnetic theory, losses due to distance have been empirically modelled, at least since the 50's [15]. Extensive campaign measurements carried out at different distances, and possibly different frequencies and terrains or building densities, indicate that distance losses can be modelled by a power law. The simplest power law model is

$$L[\text{dB}] = 10\log\left(K_1 r^n\right) = 10n\log r + K_1 \qquad (1)$$

where L is the path loss, r the distance in meters, n is the Path Loss Exponent (PLE), a parameter of the model, and K_1 can be seen as the propagation loss experienced at 1 m.

The PLE seems to account for different types of propagation environments (factories, offices, urban macrocells, urban microcells, etc.). Although it is an empirical parameter and can not be interpreted strictly as a variable that takes continuous values, higher values of n tend to show highly obstructed propagation conditions. For those cases, for example, the intuitive explanation is that the received power drops by a higher factor in a highly obstructed scenario than in one with Line of Sight (LoS)

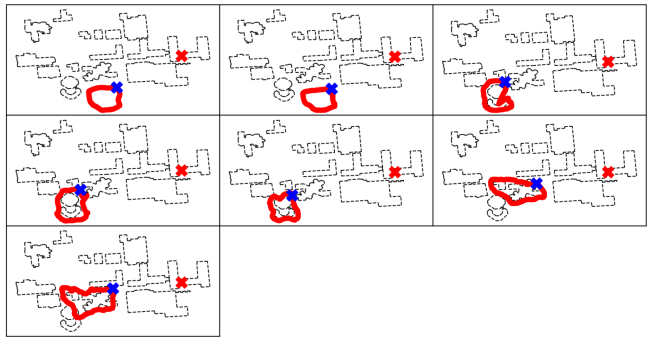

Fig. 5. Top view of transmitter measurement routes for MXW BS. The BS location, start of the route are indicated by the red cross and blue cross, respectively. By convention we designate graph in the top left as the graph (1,1). The convention used is: (row number, column number). Graph (1,1): PL route. Graph (1,2): PL route. Graph (1,3): MC route. Graph (2,1): MC route. Graph (2,2): MC route. Graph (2,3): SB route. Graph (3,1): SB route.

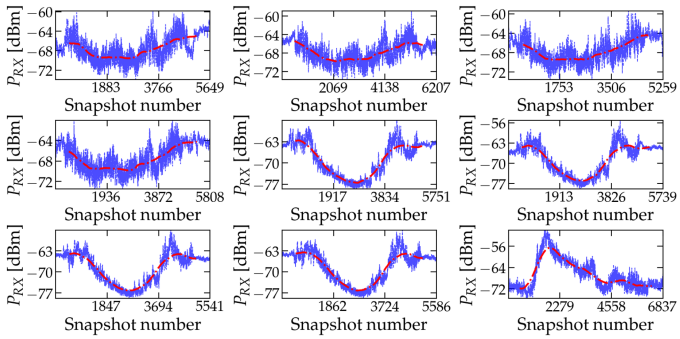

Fig. 6. Received power for all the measurements taken with MKT BS. The corresponding routes are depicted in Fig. 4. The doted red lines represent the mean functions after smoothing with a window length of $w = 1000$.

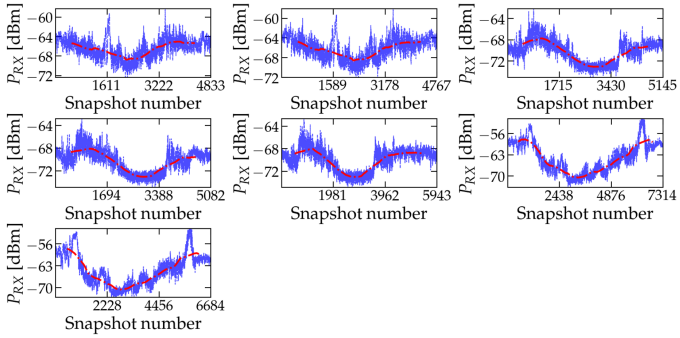

Fig. 7. Received power for all the measurements taken with MXW BS. The corresponding routes are depicted in Fig. 5. The doted red lines represent the mean functions after smoothing with a window length of $w = 1000$.

conditions, for the same distance range. From a mathematical point of view it represents the linear slope of the relationship between the received power and the distance in the $\log_{10}$ scale.

Algorithm 1 shows the procedure to find out the PLE. The procedure also produce the shadowing values (denoted in step 8 as X_{SH}) for which a separate analysis will be given in Section IV.

Received power P_{RX} computed as in step 3 of Algorithm 1 is shown in Figs. 6 and 7. There is an CIR $\mathbf{H}_t \in \mathbb{C}^{N_\tau \times N_{\text{TX}} N_{\text{RX}}}$ each $t = \frac{1}{f_{\text{IRF}}}$ seconds. CIR entries for which the square magnitude

Algorithm 1: Empirical extraction of distance-based loss and shadowing.

Input: P_{TX} [dBm], $\mathbf{H}_t \in \mathbb{C}^{N_\tau \times N_{\text{TX}} N_{\text{RX}}}$, $t = 1, \ldots, T$, smoothing window length w, noise threshold ξ

Output: n, X_{SH}

1: Remove noise floor: $\forall i, j, t \, |[\mathbf{H}]_{ijt}|^2 < \xi \rightarrow [\mathbf{H}]_{ij} =$ NaN

2: $[\mathbf{H}^{\text{NARROW}}]_{tj} = \sum_{i=1}^{N_\tau} [\mathbf{H}]_{ijt}$

3: $P_{\text{RX}}[t] = 10 \log_{10} \left(\sum_{j=1}^{N_{\text{RX}} N_{\text{TX}}} |[\mathbf{H}^{\text{NARROW}}]_{tj}|^2 \right)$

4: $L \, [dB] = P_{\text{TX}} - P_{\text{RX}}$

5: Smooth short-term losses: $L_{\text{SMOOTH}}[k] = \frac{1}{w} \sum_{t=k}^{n+D-1} L[t]$

6: Sort L_{SMOOTH} by increasing r.

7: Find $\hat{n}$: $\text{argmin}_n ||L_{\text{SMOOTH}} - 10n \log_{10} r||_2^2$

8: Find X_{SH}: $L_{\text{SMOOTH}} - 10\hat{n} \log_{10} r$

(power) is less than a noise threshold are removed. After that, all the delay contributions are added to get a narrowband CIR, and all the MIMO channels are combined.

The noise floor ξ used is -110 dBm. The smoothing window length w controls how much short-term fading is removed. Higher values of it can produce too much smoothing, which in turn might remove the medium-term losses or shadowing. Durgin [16] proposed the concept of a *local area*, for which a terminal only experiences small-scale effects. That is to say, that for such zone, distance-based losses and obstruction losses (shadowing) are not relevant. More precisely, Durgin defines the zone as the largest volume enclosing a point, for which the radio channel can be modelled as a sum of homogeneous plane waves. The upper limit of the zone is

$$\frac{L_{\text{A}}}{\lambda} < \frac{f_{\text{c}}}{B} \tag{2}$$

where L_{A} is the local area size, λ the wavelength, f_{c} the carrier frequency, and B the bandwidth. The smoothing (or moving average) step 2 in Algorithm 1 requires that the last $D-1$ samples of L_{SMOOTH} remain equal to the last $D-1$ samples of L. Equivalently, it is possible to make the first $D-1$ samples of L_{SMOOTH} equal to those of L, and the moving average will reach the end of the signal L. Using values in Table I we get $L_{\text{A}} < 19 \, \lambda$.

Step 7 in Algorithm 1 fits a mathematical model to an empirical data input. In this case, the mathematical model is linear and solely based on the data, meaning that no physical information is used. According to [30] such a path loss model is usually referred as a *Floating-Intercept* (FI) model and is defined as follows:

$$L^{\text{FI}}[\text{dB}] = b + n^{\text{FI}} 10 \log_{10} \left(\frac{d}{d_0} \right) + X_{\text{SH}}^{\text{FI}} \tag{3}$$

where the value b of L^{FI} at the initial reference distance d_0 is provided by the fit, and $X_{\text{SH}}^{\text{FI}}$ is the shadowing associated to the FI model.

On the other hand, if it is assumed that L should have a specific value for the intercept at d_0, based on physical considerations, then the model is called *Close-In* (CI) [30], and is defined as:

$$L^{\text{CI}}[dB] = \text{FSPL}(d_0) + n^{\text{CI}} 10 \log_{10} \left(\frac{d}{d_0} \right) + X_{\text{SH}}^{\text{CI}}$$

$$\text{FSPL}(d_0) = \left(\frac{4\pi d_0}{\lambda} \right)^2 \tag{4}$$

In this case the value of the intercept is decided by the Free Space Path Loss (FSPL), meaning that at the reference distance the path loss is assumed to behave as in free space. For this model the shadowing associated is denoted by $X_{\text{SH}}^{\text{CI}}$.

PLE estimated for each model, transmitter route and BS location are shown in Table II. For the *close-in* model, all the linear regression fits are imposed to pass through the point $(1, (\frac{4\pi f_{\text{c}}}{c}))^2$. Due to that, and to the fact that all observations are confined to a range of transmitter-receiver distances small (less than 50% in some cases) compared to the full range of distances (around all the observations lie in a distance range of 100 m), the PLEs for this model have all a similar value. For instance, for the routes for which the range of distances is bigger (MC and SB routes for the MKT BS have observations within a distance range of 100 m) the PLE increases its value, meaning that the lack of observations in the full range of distances or a lack of observations in a bigger range of distances might be hiding the true n^{CI} for this model. On the other hand, since the *floating-point* model does not impose an intercept for the equation of the line (b is a parameter to be estimated in (3)), the situation described previously does not occur. PLE vary enough to indicate that each route have different propagation environment. However, the cost paid by the *floating-point* model is that the estimated intercept b might not have physical meaning. For instance, for some of the routes the estimated b indicates that the path loss is very small (negative in dB) or negligible, in contradiction with the $\simeq$40 dB free space loss at 3.8 GHz and 1 m of distance. The actual values of the intercept b of the FI model are presented in Table II.

TABLE II
PATH LOSS FI MODEL PARAMETERS

BS	PL[a]	b [dB]	n^{FI}	n^{CI}	b^{AR} [dB]	$n_{\text{AR}}^{\text{FI}}$	$n_{\text{AR}}^{\text{CI}}$
MKT	1	45.5	1.93	2.08	38.8	2.21	2.08
MKT	2	46.3	1.9	2.08			
MKT	3	40.3	2.15	2.07			
MKT	4	21.5	2.95	2.07			
MXW	1	34	2.44	2.09	40	2.18	2.09
MXW	2	45.8	1.93	2.09			
BS	MC[b]	b	n^{FI}	n^{CI}	b^{AR} [dB]	$n_{\text{AR}}^{\text{FI}}$	$n_{\text{AR}}^{\text{CI}}$
MKT	1	-30	5.4	2.24	-26	5.32	2.24
MKT	2	-35.2	5.72	2.23			
MKT	3	-22.3	5.17	2.25			
MKT	4	-21.7	5.13	2.24			
MXW	1	20	3.12	2.18	17.4	3.22	2.18
MXW	2	13.3	3.41	2.19			
MXW	3	18.3	3.17	2.17			
BS	SB[c]	b	n^{FI}	n^{CI}	b^{AR} [dB]	$n_{\text{AR}}^{\text{FI}}$	$n_{\text{AR}}^{\text{CI}}$
MKT	1	-6.5	4.47	2.23	-	-	-
MXW	1	-31.6	5.29	2.01	-28.7	5.16	2.01
MXW	2	-26	5.04	2.02			

[a] PL route.
[b] MC route.
[c] SB route.

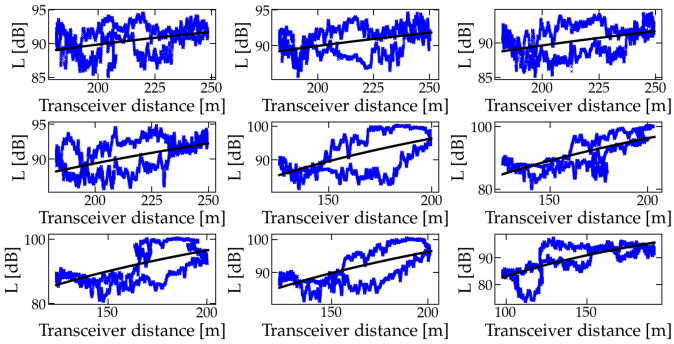

Fig. 8. Path Loss for the received power in Fig. 6 (MKT BS) with their linear fits. The linear fit uses the *floating-intercept* model.

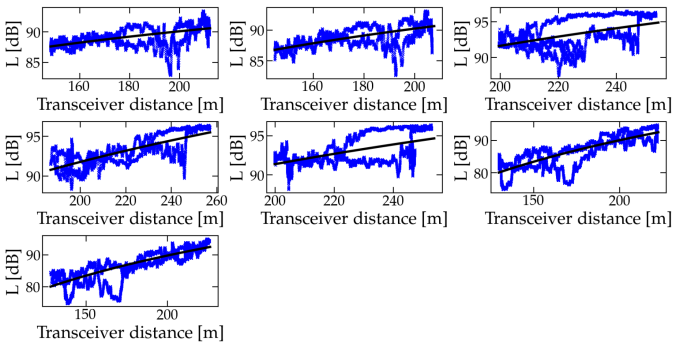

Fig. 9. Path Loss for the received power in Fig. 7 (MXW BS) with their linear fits. The linear fit uses the *floating-intercept* model.

Another bias of the linear regression fit should occur due to the lack of enough observations in the range of distances. In other words, observations at some distances might be biasing the model, since there are more available observations at those particular distances. To overcome this problem, path losses for both models are again computed using all the trials of a given route in the same fit. Here, we assume section that all trials of a route belong to the same channel, although in reality channel conditions might change between trials. In Section V-A this assumption is tested. Figs. 10 and 11 and columns b^{AR}, $n^{\mathrm{FI}}_{\mathrm{AR}}$, $n^{\mathrm{CI}}_{\mathrm{AR}}$ of Table II show path loss and PLE computed following the previous approach. Now that more observations are available for each transmitter-receiver distance bin, the linear fit is clearly a mean tendency of the path loss (see PL route with MKT BS in Fig. 10).

The scenario under analysis does not fit completely under any of the WINNER II propagation scenarios. In suburban macro-cell C1, surrounding buildings are typically residential houses up to 2 floors, while here the average is around five floors. In urban macro-cell C2, antenna height located at MKT is not clearly above all surrounding buildings, and building height is not homogeneous due to the variations of height of the terrain. For Urban and Bad Urban micro-cell B1 and B2, antenna height located at MXW is not well below the tops of surrounding buildings. Moreover, the streets grid is irregular and not Manhattan-like.

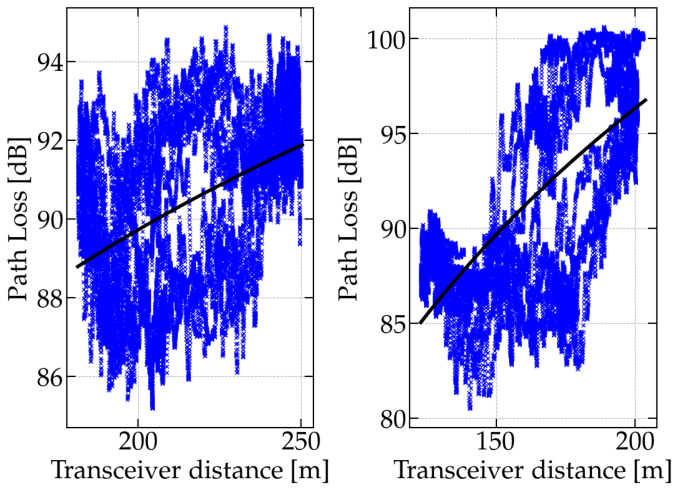

Fig. 10. Path Loss for all the received power measurements in PL (left) and MC (right) with MKT BS. Results shown for the *floating-intercept* model.

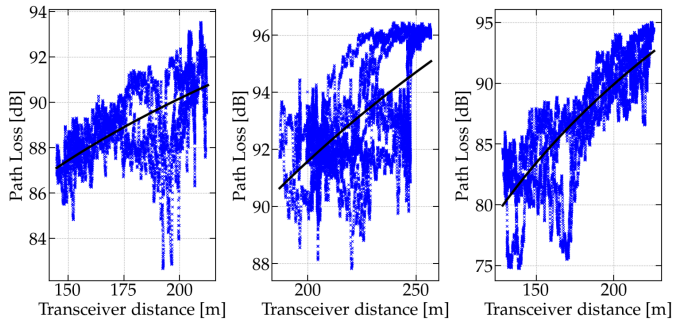

Fig. 11. Path Loss for all the received power measurements in PL (left), MC (center) and redSB (right) with MXW BS. Results shown for the *floating-intercept* model.

For an antenna height between 14–25 m (both MXW and MKT BS height are within this range) the PLE for propagation scenarios C1 and C2 ranges between 3.57 and 3.83, approximately. None of the n^{CI} is above this value. The PLE for scenarios B1 and B2 does not go upper than 2.8, which is again above all the computed n^{CI}. In WINNER II there are no propagation scenarios for which the PLE is above 4. From the perspective of WINNER II path loss models, since all computed n^{CI} are below 2.5, they correspond either to LoS or scenario B1 conditions, where antenna heights are above surrounding buildings, streets are Manhattan-like and there are open areas. However, the range of transmitter-receiver distances is below 100 m for most of the cases (and less than 60 m in some cases), meaning that path loss might be biased due to the lack of a longer range of distances.

IV. Shadowing Extraction

Shadowing variable X_{SH} is computed from step 8 in Algorithm 1. The FI path loss model is used to estimate all shadowing variables presented in this section. For simplicity we drop the superscript FI in $X^{\mathrm{FI}}_{\mathrm{SH}}$. It can be understood as a consequence of the presence of obstacles and as the remaining signal after

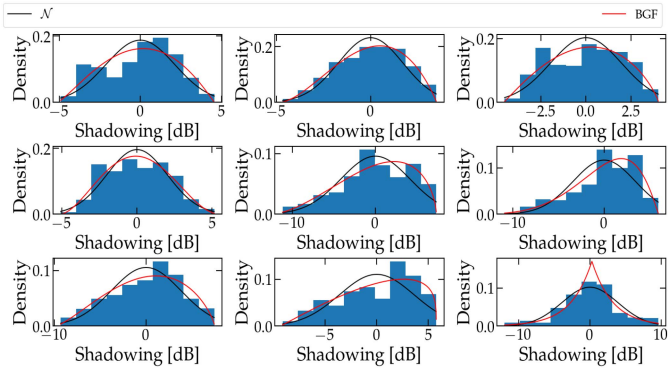

Fig. 12. Empirical distribution of shadowing for all the measurements with MKT BS. The solid black line represents a Gaussian fit with parameters shown in Table III. The solid red line represents the BGF distribution with the parameters shown in Table IV.

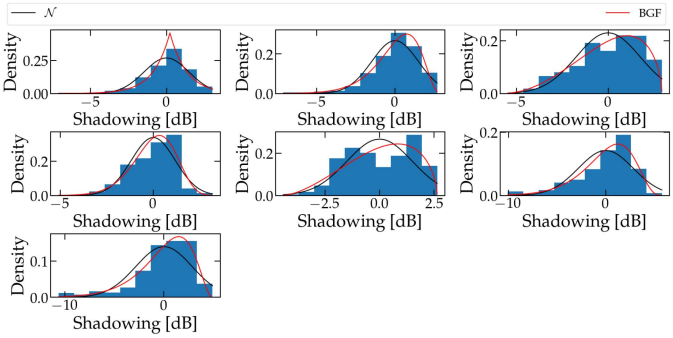

Fig. 13. Empirical distribution of shadowing for all the measurements with MXW BS. The solid black line represents a Gaussian fit with parameters shown in Table III. The solid red line represents the BGF distribution with the parameters shown in Table IV.

removing small-scale fading and subtracting the distance-based path loss. Due to its stochastic nature it has been modelled as a random variable. It is widely accepted [17], [18] that shadowing distributes according to a log-normal random variable

$$Y_{\text{SH}} = 10^{\frac{X_{\text{SH}}}{10}} \sim p_{Y_{\text{SH}}}(y), \;\; \forall y \geq 0$$

$$p_{Y_{\text{SH}}}(y) = \frac{10}{\log_e(10)\sqrt{2\pi}x\sigma_{\mathcal{N}}} \exp\left(-\frac{(10\log_{10}(y) - \mu_{\mathcal{N}})^2}{2\sigma^2_{\mathcal{N}}}\right) \tag{5}$$

or as a Gaussian in the dB scale

$$X_{\text{SH}}\ [\text{dB}] \sim p_{X_{\text{SH}}}(x) = \mathcal{N}(\mu_{\mathcal{N}}, \sigma^2_{\mathcal{N}}) \tag{6}$$

This widely accepted assumption arises from what follows. If along a path each obstacle attenuates independently the signal an amount A_i, the total attenuation due to all the obstacles in the path is $\prod_i A_i$ or $\sum_i A_i$ in the dB scale. It is easy to notice that as the number of obstacles grows, no matter which probability distribution we use to model the individual attenuations they make, the total attenuation must distribute as a Gaussian due to the Central Limit Theorem.

In reality the individual attenuations of the obstacles are not independent. There might exist correlations between some obstacles that do not allow to express the total attenuation as a product between all the obstacles. Besides that, not all the losses due to the obstacles have the same contribution in the total loss: an example are the losses close to the mobile antenna, which might have a bigger impact. Moreover, losses due to diffraction do not add up in such a way [19]. While the shadowing-Gaussian assumption is well established, there are other models for it also [20], [21].

In Figs. 12 and 13 the empirical distributions of the shadowing for all the measurements of each route and BS are shown. For each of the shadowing signals computed, two statistical tests are conducted in which we test if there is enough statistical evidence to reject or no the null hypothesis H_0. First, we test if the shadowing empirical distribution follows a Gaussian by checking if the following null hypothesis H_0 is accepted or not

$$H_0 : X_{\text{SH}} \sim \mathcal{N}(\mu_{\mathcal{N}}, \sigma^2_{\mathcal{N}}), \qquad H_1 : X_{\text{SH}} \nsim \mathcal{N}(\mu, \sigma^2) \tag{7}$$

In second place, we test if it follows a given probability distribution $p_{X_{\text{SH}}}(x)$ with three possible parameters (LOC, SCA, SHAPE)

$$H_0 : X_{\text{SH}} \sim p_{X_{\text{SH}}}(x)(LOC, SCA, SHAPE)$$
$$H_1 : X_{\text{SH}} \nsim p_{X_{\text{SH}}}(x) \tag{8}$$

from the following set of test distributions: Alpha, Beta, Gaussian, Exponential, Gamma, Laplacian, Nakagami, Rayleigh, Rician, Uniform, Gaussian Hyper-Geometric (GHG). The location parameter (LOC) controls the median location of the distribution, the scale parameter (SCA) controls the spread, and the shape parameter (SHAPE) controls the shape of the distribution for the case of skewed distributions.

For the second test, it is kept only the test probability distribution providing the Best Goodness of Fit (BGF) to the empirical distribution: the one with the lowest test statistic value. The Kolmogorov-Smirnov (KS) statistical test is used. The statistic computed by the test is [31]

$$S = \sup_x |F_{X_{\text{SH}}}(x) - F_{\text{EMP}}(x)| \tag{9}$$

where $F_{\text{EMP}}(x)$ is the empirical cumulative distribution and $F_{X_{\text{SH}}}(x)$ is the cumulative test distribution. To decide whether the null hypothesis H_0 in (8) is rejected, the statistic value is compared to a critical value that depends on the size of the sample and the desired level of significance.

Results for the Gaussian test are comprised in Table III. Given a level of significance of 0.05, all the statistic values (KS column in Table III) are above the Critical Value CV, and so the null hypothesis must be rejected. Strictly speaking, since H_0 is rejected there is no statistical evidence to say shadowing distributes as a Gaussian. Most of the empirical distributions have non-symmetrical shapes, meaning the shadowing values after and before the mode do not have the same probability of occurrence. This is expected to happen, since the route is imposing specific propagation mechanisms, that is to say: incoming signals do not combine constructively or destructively in the same amount for all the route. Estimated values for $\mu_{\mathcal{N}}$ and $\sigma^2_{\mathcal{N}}$ are shown in Table III, while the closest Gaussian to the empirical distribution is shown in Figs. 12–15.

TABLE III
GAUSSIAN FIT FOR SHADOWING

BS	PL	KS [a]	$\mu_{\mathcal{N}}$	$\sigma_{\mathcal{N}}$	CV[b]	KS	$\mu_{\mathcal{N}}$	$\sigma_{\mathcal{N}}$
MKT	1	0.067	0	2.12	0.018			
MKT	2	0.041	0	1.72	0.017	0.054	0	1.96
MKT	3	0.071	0	1.97	0.018			
MKT	4	0.059	0	2.03	0.017			
MXW	1	0.073	0	1.49	0.020	0.072	0	1.49
MXW	2	0.083	0	1.48	0.019			
BS	MC	KS	$\mu_{\mathcal{N}}$	$\sigma_{\mathcal{N}}$	CV	KS	$\mu_{\mathcal{N}}$	$\sigma_{\mathcal{N}}$
MKT	1	0.064	0	4.16	0.018			
MKT	2	0.085	0	3.41	0.018	0.069	0	3.76
MKT	3	0.083	0	3.78	0.018			
MKT	4	0.118	0	3.61	0.018			
MXW	1	0.092	0	1.74	0.019			
MXW	2	0.094	0	1.18	0.019	0.092	0	1.5
MXW	3	0.094	0	1.5	0.017			
BS	SB	KS	$\mu_{\mathcal{N}}$	$\sigma_{\mathcal{N}}$	CV	KS	$\mu_{\mathcal{N}}$	$\sigma_{\mathcal{N}}$
MKT	1	0.065	0	3.92	0.016	-	-	-
MXW	1	0.11	0	2.8	0.016	0.091	0	2.84
MXW	2	0.089	0	2.85	0.016			

[a] KS statistic value for the Gaussian fit.

[b] CV to reject the null hypothesis is equal to $\sqrt{\frac{-\log(\alpha * 0.5)}{n}}$, with a significance level of $\alpha = 0.05$ and n as the number of samples.

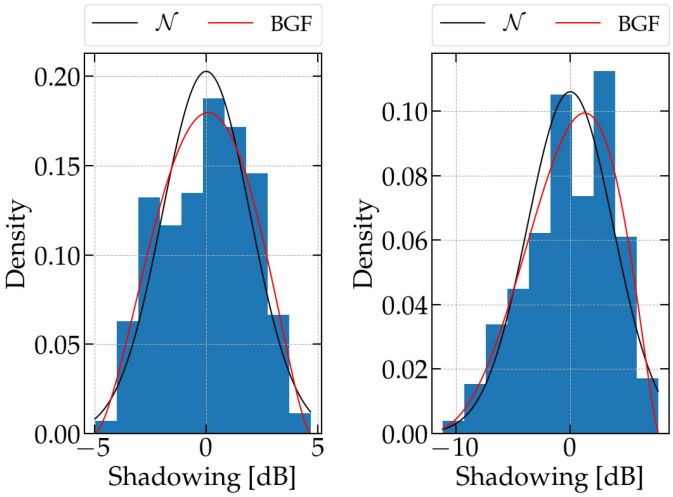

Fig. 14. Empirical distribution of shadowing with MKT BS for all PL (left) and MC (center). The solid black line represents a Gaussian fit with parameters shown in Table III. The solid red line represents the BGF distribution with the parameters shown in Table IV.

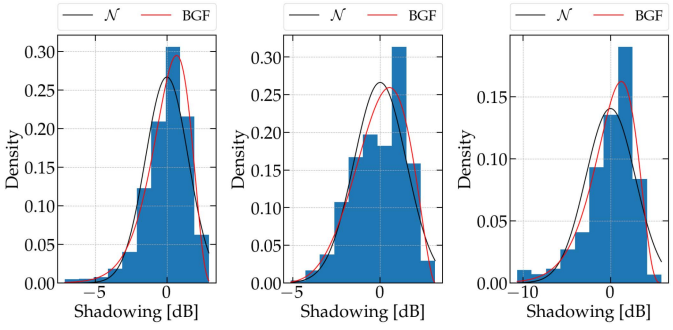

Fig. 15. Empirical distribution of shadowing with MXW BS for all PL (left), MC (center) and SB (right) routes. The solid black line represents a Gaussian fit with parameters shown in Table III. The solid red line represents the BGF distribution with the parameters shown in Table IV.

Results for the BGF test are in Table IV. Again, except for one of the measurements, none of the test distributions 'pass' the Kolmogorov-Smirnov test: the null hypothesis is rejected in all, but one, cases. Moreover, the test statistic (KS Test Statistic column in Table IV) is in some cases not much better than the test statistics for the Gaussian test. This can be appreciated in graphs of Figs. 12 and 13 for which both distributions fitted are very close.

All the measurements for a given route and BS where used as if they were coming from the same environment, similarly to what was said in Section III. Figs. 14 and 15 show the shadowing empirical distributions for this approach. It can be seen that in fact, the Gaussian fit is closer to the empirical distribution, and that the BGF fit is also close to the Gaussian fit, meaning there is no need to use another probability distribution rather than the Gaussian, at the expense of higher analytical complexity (all the BGF distributions are either Gaussian Hyper-Geometric or Beta).

V. STATIONARY ANALYSIS

A. Channel Conditions for Measurements of the Same Route

The assumption that all the measurements with the same BS and very similar transmitter routes come from the same wireless channel conditions can be tested. In reality, at least minor changes in CIRs might occur due to the fact that even for the same route, each measurement is conducted at a different moment, for which the position of obstacles as people and vehicles have changed. In [22], [23] the correlation matrix distance (CMD) measure

$$c(\mathbf{A},\mathbf{B}) = \frac{|tr(\mathbf{A}\mathbf{B}^T)|}{||\mathbf{A}||_{\mathrm{F}}||\mathbf{B}||_{\mathrm{F}}} \tag{10}$$

is used to compare the similarity between 2 matrices. In 10 $tr(\cdot)$ is the trace of a matrix and $||\cdot||_{\mathrm{F}}$ the Frobenius norm. Another definition of the CMD can be found in [24]. The CMD can be used by comparing channel matrices $\mathbf{H}_t^{\mathrm{MEAS}-1}, \mathbf{H}_t^{\mathrm{MEAS}-2}$ at time snapshot t for 2 measurements of the same route. However, since for even small changes in phase the complex gains in both matrices vary in a noticeable manner, the CMD will mostly have a low value when using instantaneous channel matrices. A solution to overcome such a situation is to average channel matrices over a time snapshot interval. Another approach would be to use instead, one of the spatial correlation matrices $\mathbf{R}_{\mathrm{TX}} = \mathbb{E}[\mathbf{H}^T(\mathbf{H}^T)^*]$, $\mathbf{R}_{\mathrm{RX}} = \mathbb{E}[\mathbf{H}\mathbf{H}^*]$ or $\mathbf{R}_{\mathrm{FULL}} = \mathbb{E}[\mathrm{vec}\,(\mathbf{H})\,\mathrm{vec}(\mathbf{H})^*]$, to test if local propagation characteristics vary [23]. In order to do so, we assume ergodicity, and so, replace the ensemble averages with time averages. A question must be arising at this point: why not, instead of assuming ergodicity, average over the available measurements of the same route, since each one could be seen as a realization of the same stochastic process. There are two answers. First: precisely, what we are trying to see is if all these measurements with the same BS and very similar routes, are referring to the same stochastic process, or in other words, to the same channel conditions. Second: there are not enough measurements for a route to average.

TABLE IV
BEST GOODNESS OF FIT (BGF) DISTRIBUTION FOR SHADOWING

BS	PL	Distribution	KS Test Statistic	Location	Scale	Shape
MKT	1	GHG[a]	0.054	-4.96	9.58	$a = 1.85, b = 2.7, c = 1.76, z = -0.79$
MKT	2	Beta	0.018	-4.8	8.3	$a = 2.69, b = 1.96$
MKT	3	GHG	0.046	-4.65	8.67	$a = 2.67, b = 1.68, c = 1.64, z = 2.13$
MKT	4	Beta	0.04	-5.18	10.75	$a = 2.95, b = 3.16$
MXW	1	GHG	0.028	-166.7	169.6	$a = 167.7, b = 3.9, c = -116.6, z = 0.8$
MXW	2	GHG	0.031	-122.3	126	$a = 164.7, b = 6.9, c = 4.6, z = -0.97$
BS	MC	Distribution	KS Test Statistic	Location	Scale	Shape
MKT	1	Beta	0.045	-12.7	20	$a = 2.77, b = 1.6$
MKT	2	Beta	0.043	-17.9	23.8	$a = 6.31, b = 2.1$
MKT	3	GHG	0.043	-9.47	17	$a = 1.92, b = 2, c = 1.6, z = -0.57$
MKT	4	GHG	0.056	-9.2	15	$a = 1.72, b = 1.76, c = 1, z = -0.89$
MXW	1	GHG	0.039	-6.64	9.58	$a = 4, b = 1.29, c = -0.45, z = -1$
MXW	2	Beta	0.068	-4358.1	4362.4	$a = 13261.8, b = 12.9$
MXW	3	GHG	0.055	-4.49	7.13	$a = 2.79, b = 1.58, c = 0.26, z = 0.9$
BS	SB	Distribution	KS Test Statistic	Location	Scale	Shape
MKT	1	Laplace	0.056	0.28	2.94	-
MXW	1	GHG	0.033	-16.2	22.7	$a = 1.63, b = 12.33, c = 21.87, z = -0.82$
MXW	2	GHG	0.028	-12.5	18.29	$a = 1.15, b = 10.43, c = 17.67, z = -0.83$

[a] Gaussian Hyper-Geometric.

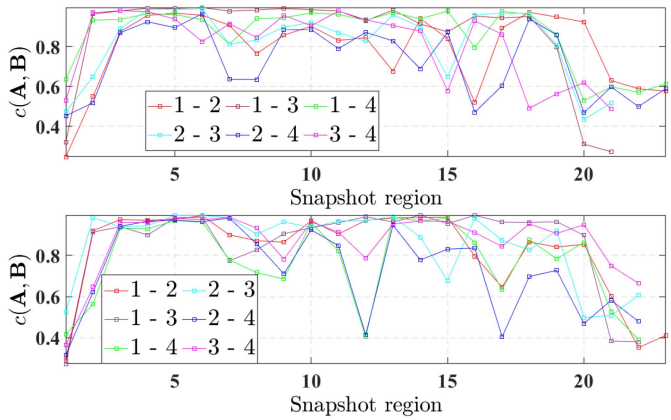

Fig. 16. CMD with MKT BS. Top panel: PL route measurements. Bottom panel: MC route measurements. $\mathbf{R}_{\text{TX}}$ matrices used for the CMD, with $w_{\text{ERGOD}} = 150\lambda$. The legend numbers $i - j$ represent the measurement i and j for the route considered. Example: $1 - 2$, means measurements 1 and 2 of the given route were used to compute the CMD.

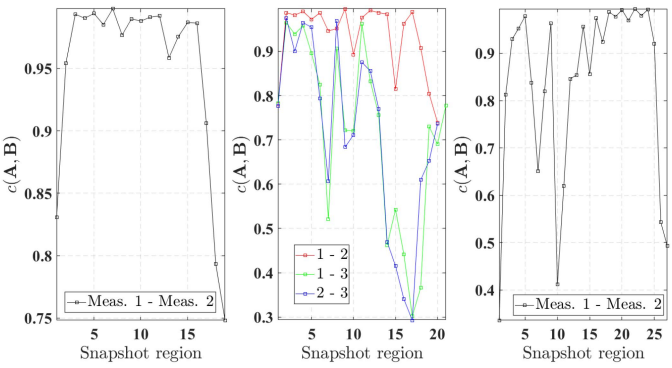

Fig. 17. CMD with MXW BS. Left panel: PL route measurements. Central panel: MC route measurements. Right panel: SB route measurements. $\mathbf{R}_{\text{TX}}$ matrices used for the CMD, with $w_{\text{ERGOD}} = 150\lambda$. The legend numbers $i - j$ represent the measurement i and j for the route considered. Example: $1 - 2$, means measurements 1 and 2 of the given route were used to compute the CMD.

For the transmitter spatial correlation matrix $\mathbf{R}_{\text{TX}}$ we define disjoint snapshot regions of size w_{ERGOD} over which we average, to obtain the following estimate of $\mathbf{R}_{\text{TX},i}$ over snapshot region i

$$\mathbf{R}_{\text{TX}} = \mathbb{E}\left[\mathbf{H}^T \left(\mathbf{H}^T\right)^*\right]$$

$$\mathbf{R}_{\text{TX},i} = \sum_{t=(i-1)*w_{\text{ERGOD}}+1}^{i*w_{\text{ERGOD}}} \mathbf{H}_t^T \left(\mathbf{H}_t^T\right)^*, \quad i = 1, \ldots, \left\lfloor \frac{N_T}{w_{\text{ERGOD}}} \right\rfloor \tag{11}$$

with N_T the number of snapshots available in the measurement, and $\lfloor \cdot \rfloor$ the function that aproximates to the lowest integer. Figs. 16 and 17 show the CMD between measurements of the same route, for each route and each BS. Regions of size $w_{\text{ERGOD}} = 150\lambda$ were used, such that there are enough CIRs available for the average in (11).

Both panels in Fig. 16 show similar aspects. First, for the beginning and end of the MC and PL routes the CMD is low. It means that for this snapshot regions, the multiple measurements of each route have non-negligible differences in propagation conditions. Differences in the measurement routes are noticeable or there are changes in propagation conditions due to, for example, the presence of new obstacles. Second, the CMD remains high (bigger than 0.5) for more than half of the snapshot regions (see snapshot regions 2 to 11, on both panels). This means it could be said that for long segments of the route the measurements belong to the same environment, which intuitively was the conclusion. Third, the graphs show high variability at snapshot regions 14 to 20, specially for the PL case. The propagation conditions must change in fact, since for these snapshot regions the transmitter coordinates of the different route trials are very similar: the average difference between the transmitter locations for the PL route trials is less than 1 m.

On the other hand, in Fig. 17 the measurements for MXW BS show different results. The available 2 measurements for the PL route are quite similar. The CMD is always above 0.6, and for most of the time above 0.8. The 2 measurements available for the

SB route also exhibit a high similarity for most of the snapshot regions. However, it is evident that the similarity in the case of the SB route is lower in average than in the PL route. This might be due to the mechanism of propagation mostly operating in the PL case. While there are no clear mechanisms of propagation for some snapshot regions of the SB route, it is clear that most of the radio signals departure at PL and arrive at MXW BS through the rooftops of the SB and Vinci buildings.

B. Stationary Regions

A stationarity region $\mathcal{SR}$ is a region for which two conditions are fulfilled. First, that the mean of the stochastic process does not vary

$$\mathcal{SR} = \{t \mid \mathbb{E}[X(t)] = \text{CONSTANT VALUE}\} \tag{12}$$

and second, that the covariance function defined by

$$\mathbb{COV}[t_1, t_2] = \mathbb{E}[(X(t_1) - \mathbb{E}[X(t_1)])(X(t_2) - \mathbb{E}[X(t_2)])] \tag{13}$$

does not depend on the specific time instants within the region, but rather, on the difference between such instants:

$$\mathcal{SR} = \{t_1, t_2 \mid \mathbb{COV}[t_1, t_2] = \mathbb{COV}[t_2 - t_1, 0]\} \tag{14}$$

If both conditions are fulfilled, the signal $X(t)$ for which the stationary regions are found is said to be stationary in the *wide-sense*. The challenge is to solve the problem of splitting the initial set of time-snapshots $\mathcal{T}_0 = \{1, 2, \ldots, T\}$ into disjoint sets $\mathcal{SR}_1, \mathcal{SR}_2, \ldots, \mathcal{SR}_{N_{\text{SR}}}$ over which conditions (12) and (14) are fulfilled. Neither the number of regions or the size of each region is known.

Different approaches have been proposed to solve the problem. However, all of them rely on looking for similarities of what can be called a summary function, capable of summarize information about the channel at different space locations or time samples. In [25], the authors use the *local scattering function* defined by Matz [26], [27] as this summary function. In [28], the spatial correlation matrices are used, and in [29] the PDP. The idea behind the algorithms presented in those references is to compare sliding portions of the summary function to check when the similarity passes or undergoes a given threshold.

Spatial correlation matrices provide information about the CIR and can be used as this summary function [28]. We can assume that for a window w_{ERGOD} of time snapshots ergodicity holds, and estimate the full spatial correlation matrix starting from a given time instant t_1 for such window w_{ERGOD} of snapshots. Then, estimate a second spatial correlation matrix starting from the time instant $t_1 + n_{\text{STEP}}$ and compare the two spatial correlation matrices by using the CMD, until it undergoes a given threshold. If the CMD does not undergo the threshold, then the parameter n_{STEP} is increased. Algorithm 2 describes all the computing steps involved. Choosing n_{STEP} imposes a trade-off: higher values speed-up the computation process at the price of merging smaller regions into bigger regions, which results in stationary regions bigger than expected. On the other hand, the threshold parameter controls on average how big are the stationary regions. Lower value allows less similar correlation matrices to be considered similar.

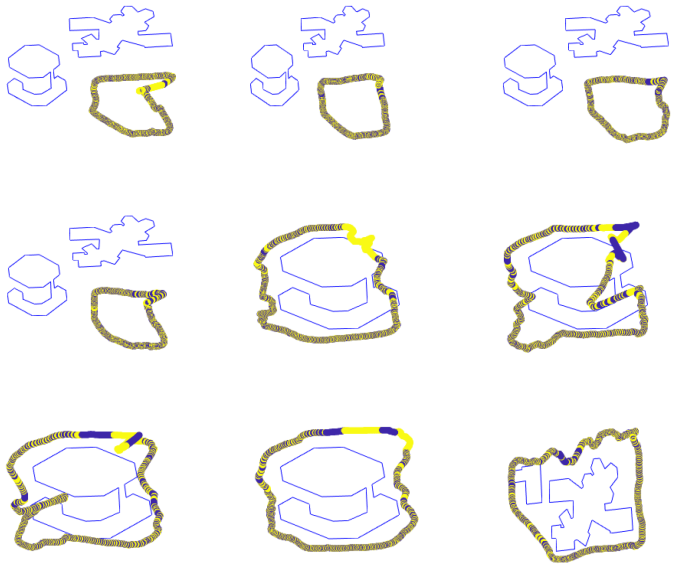

Fig. 18. Stationary regions found using Algorithm 2 for all the measurements and routes with MKT BS. Threshold level for the CMD to 0.7. The 2 colors used (blue and yellow) do not have by themselves any meaning, but are used to differentiate one region from the next one.

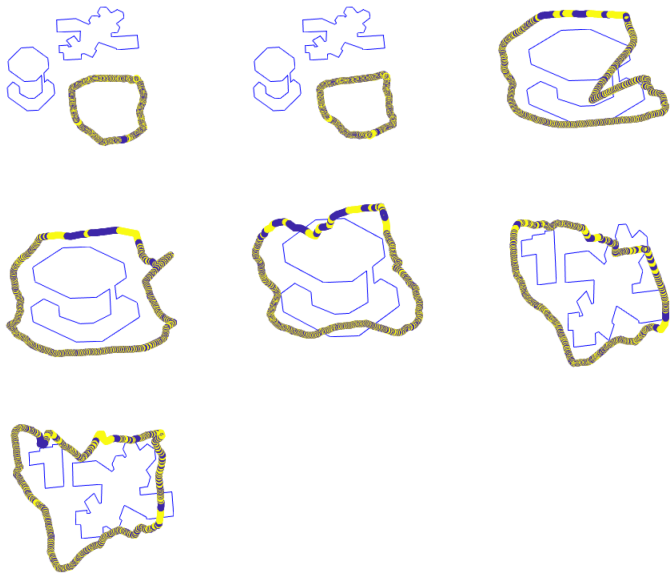

Fig. 19. Stationary regions found using Algorithm 2 for all the measurements and routes with MXW BS. Threshold level for the CMD is set to 0.7. The 2 colors used (blue and yellow) do not have by themselves any meaning, but are used to differentiate one region from the next one.

Stationary regions using this algorithm are shown in Fig. 18 and Fig. 19 for a CMD of 0.7. For the MKT BS, all the PL routes have their biggest stationary regions located in the right corner of the route. This section of the route is located behind the SB building, and is indicating that propagation there is mostly occurring through the rooftop of SB building, as otherwise, losses due to the SB building attenuate completely the radio waves. The SB and MC routes show large stationary regions for zones where there are either LoS or Obstructed Light-of-Sight (OLoS) conditions due to presence of trees between MKT BS

Algorithm 2: Methodology to compute stationary regions from spatial correlation matrix.

Input: $\mathbf{H}_t \in \mathbb{C}^{8\times 8}$, $t \in \mathcal{T}_0$, w_{ERGOD}, THR, n_{STEP}, $\mathcal{T}_0$
Output: $\mathcal{SR}_1, \mathcal{SR}_2, \ldots, \mathcal{SR}_{N_{\text{SR}}}$

1: $t_1 \leftarrow 1, k \leftarrow 1$
2: $t_2 \leftarrow t_1 + n_{\text{STEP}}$
3: **if** $t_2 + w - 1 < |\mathcal{T}_0|$ **then**
4: Get $\mathcal{T}_1 = \{t_1, t_1 + 1, \ldots, t_1 + w - 1\}$
5: Get $\mathcal{T}_2 = \{t_2, t_2 + 1, \ldots, t_2 + w - 1\}$
6: Compute: $\hat{\mathbf{R}}_1 = \frac{1}{w} \sum_{t\in\mathcal{T}_1} \text{vec}\,(\mathbf{H}_t)\,\text{vec}(\mathbf{H}_t)^H$
7: Compute: $\hat{\mathbf{R}}_2 = \frac{1}{w} \sum_{t\in\mathcal{T}_2} \text{vec}\,(\mathbf{H}_t)\,\text{vec}(\mathbf{H}_t)^H$
8: $\alpha \leftarrow c(\hat{\mathbf{R}}_1, \hat{\mathbf{R}}_2)$ (10)
9: **if** $\alpha <$ THR **then**
10: $\mathcal{SR}_k \leftarrow \{t_1, t_1 + 1, \ldots, t_2\}$
11: $t_1 \leftarrow t_2$
12: $k \leftarrow k + 1$
13: Go to step 2
14: **else**
15: $t_2 \leftarrow t_2 + n_{STEP}$
16: Go to step 4
17: **else**
18: return $\mathcal{SR}_1, \ldots, \mathcal{SR}_{N_{\text{SR}}}$

and the transmitter. The sections in the MC route are located in the Place Pierre Curie, some of which are in OLoS with the MKT BS. The section in the SB route, located in Ramps 1 and 2 in the Rue Archimède are in OLoS, due to the barrier of trees in front of MKT building.

On the other hand, for the MXW BS, LoS propagating conditions in SB route are the responsible for some of the stationary regions located in Rue Archimède. For the stationary regions of SB route located on the Place Saint Barbe, it is clear that radio waves are bouncing repeated times between SB and Vinci buildings, creating a similar effect of what is observed in a tunnel. This assumption is checked by computing the path loss for the received power when the transmitter is passing through Vinci and SB buildings (Place Saint Barbe). For this section the PLE is 2.02, indicating a clear 'tunnel' effect, as its value is close to free space PLE. For the MC routes, it is more challenging to know which propagation mechanisms are producing the long stationary regions at Place Pierre Curie, since the route is located in Non Line-of-Sight (NLoS) conditions all the time. The fact that there is an increment in received power corresponding to this regions (Graphs (1,3), (2,1) and (2,2) of Fig. 7) is showing this mechanism is clearly the responsible for all energy to arrive at the highest levels for this route. As there are NLoS conditions, some combination between diffraction through SB building rooftop and reflections coming from Ramps 1 and 2 in Rue Archimède, could led to this situation.

VI. Conclusion

From a measurement campaign at Louvain-la-Neuve with both LoS and NLoS conditions, large scale propagation parameters of interest as PLE and shadowing distribution have been computed. Both *closed-in* and *floating-point* models show the MC routes with MKT BS as having the biggest PLE, due to the obstruction of the Bibliothèque des Sciences (nowdays Musée L) which is taller than all surrounding buildings, including MKT. The drop in the received power, specially due to this building is high. For many of the *closed-in* path loss models the PLE remains within the range 2–2.5, showing they all can be considered as belonging to a similar environment: micro-cell with average building heights comparable but lower than the antenna BS height, except for the Bibliothèque des Sciences building.

Although the shadowing empirical distributions did not pass the Kolmogorov-Smirnov test for being considered as Gaussian, most of the BGF distributions neither. The complexity of the BGF distributions (many of them Gaussian Hyper-Geometric) does not justify their use to model shadowing distribution, since the Gaussian fits are very similar with a lower mathematical complexity for the function. This non-Gaussian are non-symmetrical possibly due to the bias imposed by having more observations for certain transmitter-receiver distance bins.

Finally, computed stationary regions show in average that longer regions are due to the channel coherence gained by having a strong mechanism of propagation in comparison to other regions, typically LoS or similar-to-tunnel propagation conditions.

References

[1] METIS, "METIS channel models," Tech. Rep. D1.4 v1, Feb. 2015. [Online]. Available: https://metis2020.com/wp-content/uploads/deliverables/METIS_D1.4_v1.0.pdf

[2] L. Liu et al., "The COST 2100 MIMO channel model," *IEEE Wireless Commun.*, vol. 19, no. 6, pp. 92–99, Dec. 2012.

[3] M. Zhu, G. Eriksson, and F. Tufvesson, "The COST 2100 channel model: Parameterization and validation based on outdoor MIMO measurements at 300 MHz," *IEEE Trans. Wireless Commun.*, vol. 12, no. 2, pp. 888–897, Feb. 2013.

[4] F. Ademaj, M. Taranetz, and M. Rupp, "3GPP 3D MIMO channel model: A holistic implementation guideline for open source simulation tools," *EURASIP J. Wireless Commun. Netw.*, vol. 2016, no. 1, pp. 1–14, Feb. 2016. [Online]. Available: https://jwcn-eurasipjournals.springeropen.com/track/pdf/10.1186/s13638-016-0549-9.pdf

[5] B. Mondal et al., "Qinglin and others, 3D channel model in 3GPP," *IEEE Commun. Mag.*, vol. 53, no. 3, pp. 16–23, Mar. 2015.

[6] 3GPP, "Study on channel model for frequencies from 0.5 to 100 GHz," Tech. *Rep. D38.901 v14.3.0 Release 14*, Jan. 2018.

[7] F. Burkhardt, S. Jaeckel, E. Eberlein, and R. Prieto-Cerdeira, "QuaDRiGa: A MIMO channel model for land mobile satellite," in *Proc. IEEE 8th Eur. Conf. Antennas Propag.*, Hague, The Netherlands, 2014, pp. 1274–1278.

[8] C. X. Wang, J. Bian, J. Sun, W. Zhang, and M. Zhang, "A survey of 5G channel measurements and models," *IEEE Commun. Surveys Tuts.*, vol. 20, no. 4, pp. 3142–3168, Oct.–Dec. 2018.

[9] A. Shumacher, R. Merz, and A. Burg, "3.5 GHz coverage assessment with a 5G testbed," in *Proc. IEEE 89th Veh. Technol. Conf.*, Kuala Lumpur, Malaysia, 2019, pp. 1–6.

[10] C. Oestges, N. Dementieva, and E. Vinogradov, "Evaluation of large-scale parameters in urban microcells at 3.8 GHz," in *Proc. IEEE 32nd Gen. Assem. Sci. Symp. Int. Union Radio Sci.*, Montreal, Canada, 2017, pp. 1–2.

[11] M. C. Walden and F. J. Rowsell, "Urban propagation measurements and statistical path loss model at 3.5 GHz," in *Proc. IEEE Antennas Propag. Soc. Int. Symp.*, 2005, pp. 363–366.

[12] W. Joseph, L. Roelens, and L. Martens, "Path loss model for wireless applications at 3500 MHz," in *Proc. IEEE Antennas Propag. Soc. Int. Symp.*, 2006, pp. 4751–4754.

[13] "Propagation data and prediction methods for the planning of short-range outdoor radiocommunication systems and radio local networks in the frequency range 300 MHz to 100GHz," ITU-R, Tech. Rep. Recommendation P. 1411–9, Jun. 2017.

[14] J. D. Villegas, "Non-stationary spatial shadowing models for micro-cellular radio links," Ph.D. dissertation, Inst. Inf. Commun. Technol. Electron. Appl. Math., UCLouvain, Ottignies-Louvain-la-Neuve, Belgium, Oct. 2021.
[15] J. J. Egli, "Radio propagation above 40 MC over irregular terrain," *Proc. IRE*, vol. 45, no. 10, pp. 1383–1391, Oct. 1957.
[16] G. D. Durgin, "Theory of stochastic local area channel modeling for wireless communications," Ph.D. dissertation, Elect. Comput. Eng. Fac., Virginia Polytech. Inst. State Univ., Blacksburg, VA, USA, Nov. 2000.
[17] J. Liberti and T. Rappaport, "Statistics of shadowing in indoor radio channels at 900 and 1900 MHz," in *Proc. MILCOM Conf. Rec.*, San Diego, USA, Oct. 1992, pp. 1066–1070.
[18] A. J. Goldsmith, L. J. Greenstein, and G. J. Foschini, "Error statistics of real-time power measurements in cellular channels with multipath and shadowing," *IEEE Trans. Veh. Technol.*, vol. 43, no. 3, pp. 439–446, Aug. 1994.
[19] S. R. Saunders and A. Aragón-Zavala, *Antennas and Propagation for Wireless Communication Systems*. Chichester, West Sussex, U.K.: Wiley, 2007.
[20] A. Abdi and M. Kaveh, "On the utility of gamma PDF in modeling shadow fading (slow fading)," in *Proc. IEEE 49th Veh. Technol. Conf.*, Houston, USA, 1999, pp. 2308–2312.
[21] P. M. Shankar, "Macrodiversity and microdiversity in correlated shadowed fading channels," *IEEE Trans. Veh. Technol.*, vol. 58, no. 2, pp. 727–732, Feb. 2009.
[22] N. Czink, B. Bandemer, G. Vazquez-vilar, L. Jalloul, and A. Paulraj, "Can multi-user MIMO measurements be done using a single channel sounder?," in *Proc. COST 2100 6th Manage. Committee Meeting*, Lille, France, TD, Oct. 2008, pp. 6–8.
[23] M. Herdin, N. Czink, H. Ozcelik, and E. Bonek, "Correlation matrix distance, a meaningful measure for evaluation of non-stationary MIMO channels," in *Proc. IEEE 61st Veh. Technol. Conf.*, Stockholm, Sweden, 2005, pp. 136–140.
[24] X. Ge, R. Zi, H. Wang, J. Zhang, and M. Jo, "Multi-user massive MIMO communication systems based on irregular antenna arrays," *IEEE Trans. Wireless Commun.*, vol. 15, no. 8, pp. 5287–5301, Aug. 2016.
[25] A. Paier et al., "Non-WSSUS vehicular channel characterization in highway and urban scenarios at 5.2 GHz using the local scattering function," in *Proc. IEEE Int. ITG Workshop Smart Antennas*, Darmstadt, Germany, 2008, pp. 9–15.
[26] G. Matz, "Doubly underspread non-WSSUS channels: Analysis and estimation of channel statistics," in *Proc. IEEE 4th Workshop Signal Process. Adv. Wireless Commun. (IEEE Cat. No.03EX689)*, Rome, Italy, 2003, pp. 190–194.
[27] G. Matz, "On non-WSSUS wireless fading channels," *IEEE Trans. Wireless Commun.*, vol. 4, no. 5, pp. 2465–2478, Sep. 2005.
[28] O. Renaudin, V. M. Kolmonent, P. Vainikainent, and C. Oestges, "Impact of correlation matrix estimation accuracy on the computation of stationarity intervals," in *Proc. IEEE 4th Eur. Conf. Antennas Propag.*, Barcelona, Spain, 2010, pp. 1–5.
[29] A. Gehring, M. Steinbauer, I. Gaspard, and M. Grigat, "Empirical channel stationarity in urban environments," in *Proc. 4th Eur. Pers. Mobile Commun. Conf.*, Vienna, Austria, 2001. [Online]. Available: https://publik.tuwien.ac.at/files/pub-et_12758.pdf
[30] S. Sun et al., "Propagation path loss models for 5G urban micro- and macro-cellular scenarios," in *Proc. IEEE 83rd Veh. Technol. Conf.*, Nanjing, China, 2016, pp. 1–6.
[31] J. R. Lanzante, "Testing for differences between two distributions in the presence of serial correlation using the kolmogorov–smirnov and kuiper's tests," *Int. J. Climatol.*, vol. 41, no. 14, pp. 6314–6323, Nov. 2021.

Julian David Villegas Gutierrez (Member, IEEE) received the bachelor's and master's degrees in electronics engineering from the Universidad de los Andes, Bogota, Colombia, in 2012 and 2015, respectively, and the Ph.D. degree in sciences de l'ingénieur et technologie from the Université Catholique de Louvain, Louvain-la-Neuve, Belgium, in 2021. From 2016 to 2017, he was a Research Assistant with the Department of Electrical Engineering, Universidad de los Andes, Bogota, Colombia. His research interests include statistical analysis and machine learning applied to wireless communications.

Claude Oestges (Fellow, IEEE) received the M.Sc. and Ph.D. degrees in electrical engineering from the Université catholique de Louvain (UCLouvain), Louvain-la-Neuve, Belgium, respectively, in 1996 and 2000. In January 2001, he joined as a Postdoctoral Scholar the Smart Antennas Research Group (Information Systems Laboratory), Stanford University, Stanford, CA, USA. From January 2002 to September 2005, he was associated with the Microwave Laboratory UCLouvain as a Post-doctoral Fellow of the Belgian Fonds de la Recherche Scientifique (FRS-FNRS). Claude Oestges is currently Full Professor with the Electrical Engineering Department, Institute for Information and Communication Technologies, Electronics and Applied Mathematics (ICTEAM), UCLouvain. He was the Chair of COST Action CA15104 IRACON (2016-2020). He is the author or co-author of three books and more than 200 journal papers and conference communications. He was the recipient of the 1999–2000 IET Marconi Premium Award and of the IEEE Vehicular Technology Society Neal Shepherd Award in 2004 and 2012.